

# Zn/Pt dual-site single-atom driven difunctional superimposition-augmented sonosensitizer for sonodynamic therapy boosted ferroptosis of cancer

Received: 8 July 2023

Accepted: 14 October 2024

Published online: 29 October 2024

 Check for updatesDing Wen <sup>1,2</sup>, Jing Feng <sup>1,2</sup> , Ruiping Deng <sup>1</sup>, Kai Li <sup>1</sup>  & Hongjie Zhang <sup>1,2,3</sup> 

Sonodynamic therapy (SDT) as a non-invasive antitumor strategy has been widely concerned. However, the rapid electron ( $e^-$ ) and hole ( $h^+$ ) recombination of traditional inorganic semiconductor sonosensitizers under ultrasonic (US) stimulation greatly limits the production of reactive oxygen species (ROS). Herein, we report a unique Zn/Pt dual-site single-atom driven difunctional superimposition-augmented  $TiO_2$ -based sonosensitizer (Zn/Pt SATs). Initially, we verify through theoretical calculation that the strongly coupled Zn and Pt atoms can assist electron excitation at the atomic level by increasing electron conductivity and excitation efficiency under US, respectively, thus effectively improving the yield of ROS. Additionally, Zn/Pt SATs can significantly enhance ferroptosis by producing more ROS and sonoexcited holes under US stimuli. Therefore, the establishment of dual-site single-atom system represents an innovative strategy to enhance SDT in cancer model of female mice and provides a typical example for the development of inorganic sonosensitizer in the field of antitumor therapy.

Sonodynamic therapy (SDT) is a non-invasive treatment method, in which sonosensitizer could produce toxic reactive oxygen species (ROS) under ultrasound (US) stimuli to achieve tumor suppression<sup>1–4</sup>. Compared with photodynamic therapy (PDT), SDT with deeper tissue penetration could effectively target tumors in deep tissues for effective inhibition<sup>5–8</sup>. Due to the low-yield ROS generation of sonosensitizer and the complexity of tumors, SDT is still in its infancy and has not yet achieved widespread clinical translation<sup>9–12</sup>. Therefore, to improve the ROS generation ability of promising sonosensitizers and break through the major limitation of low-yield ROS generation are extremely important to realize effective SDT for future primary antitumor therapy<sup>13–16</sup>. Inorganic semiconductor sonosensitizers have been widely studied due to their unique physical and chemical properties,

and excellent biocompatibility<sup>17–20</sup>. However, it is easy to recombine electron-hole pairs under US stimuli, which greatly limits ROS production and extremely reduces the therapeutic effect of SDT<sup>21–24</sup>. In view of this problem, many strategies for improving the separation efficiency of electron-hole pairs in inorganic semiconductor sonosensitizers have been developed, such as combining with noble metals, creating more oxygen defects on sonosensitizers, and combining with hole trapping agents<sup>25–28</sup>. However, these strategies focus on the enhancement of electron-hole pair separation efficiency by a single component, while the synergistic mechanism between different components at the atomic level is basically ignored. Therefore, the key to improving the separation efficiency of electron-hole pairs of sonosensitizer is to perfect the design of sonosensitizer system and

<sup>1</sup>State Key Laboratory of Rare Earth Resource Utilization, Changchun Institute of Applied Chemistry, Chinese Academy of Sciences, 130022 Changchun, China. <sup>2</sup>University of Science and Technology of China, 230026 Hefei, China. <sup>3</sup>Department of Chemistry, Tsinghua University, 100084 Beijing, China. ✉ e-mail: [fengji@ciac.ac.cn](mailto:fengji@ciac.ac.cn); [likai@ciac.ac.cn](mailto:likai@ciac.ac.cn); [hongjie@ciac.ac.cn](mailto:hongjie@ciac.ac.cn)

rationally utilize the synergistic effect of atomic-level electronic structure regulation.

Single-atom nanoplatforms have attracted tremendous attention due to the utilization efficiency maximization of metal atoms<sup>29–33</sup>. At the same loading, the group in the form of a single atom exposes more active sites, which makes the single-atom nanoplatforms have more excellent properties<sup>34–36</sup>. It is worth noting that the dual-site single-atom systems with two kinds of metal atoms located at neighboring positions can cooperate in the chemical transformation to generate the synergistic effect, and often show better electronic regulatory properties than the typical single-atom systems<sup>37</sup>. The unique characteristics of dual single-atom system give it unexpected high performance, and it has been successfully applied in the fields of thermal catalysis, electrocatalysis, and biocatalysis<sup>38–40</sup>. Especially in the field of biocatalysis, dual single-atom has been widely concerned because of its high catalytic activity of nanozyme<sup>41</sup>. So far, there have been few reports on the regulation of SDT by dual-site single-atom systems.

Herein, we develop a Zn/Pt dual-site single-atom loaded TiO<sub>2</sub> sonosensitizer (Zn/Pt SATs) with rich oxygen defects for Zn/Pt driven difunctional superimposition-augmented SDT (Fig. 1). Under US stimuli, the Zn single-atoms and Pt single-atoms play two different roles to assist electron excitation of Zn/Pt SATs. Specifically, the introduction of Zn increases the electronic conductivity of the system and that of Pt leads to the formation of impurity bands in the band gap. Therefore, the presence of Zn can increase the electron transport capacity of the system.

Meanwhile, electrons in the conduction band excited from Pt-5d orbital can also be activated, which results in the improvement of excitation efficiency and increases the activation efficiency of O<sub>2</sub> and H<sub>2</sub>O. This process can effectively improve the separation efficiency of electron-hole pairs, so as to achieve efficient SDT. In addition, Zn/Pt SATs with dual single-atom structure give it catalase (CAT)-like and peroxide (POD)-like activities. Zn/Pt SATs with CAT-like activity could effectively alleviate tumor hypoxia, thereby enhancing the singlet oxygen (<sup>1</sup>O<sub>2</sub>) production efficiency during SDT. The POD-like activity of Zn/Pt SATs contributes to the continuous production of hydroxyl radicals ( $\cdot$ OH) in the system. In addition to depleting glutathione (GSH) by Zn/Pt SATs itself, the sonoexcited holes can also deplete GSH, which greatly improves the GSH consumption capacity of Zn/Pt SATs under US stimuli. The intrinsic GSH degradation capacity and POD-like activity of Zn/Pt SATs could lead to the down-regulation of glutathione peroxidase 4 (GPX4) protein and a large accumulation of lipid peroxides (LPO), thus inducing ferroptosis. Furthermore, the sonoexcited holes and ROS produced by Zn/Pt SATs under the US contribute to sono-boostered ferroptosis. Consequently, enviable oncotherapy results could be obtained due to the innovational charge separation optimization in SDT and sono-boostered ferroptosis. This work presents an example of the synergistic effect between dual single-atom structures on charge separation optimization, and elucidates the application of dual-site single-atom systems in SDT.

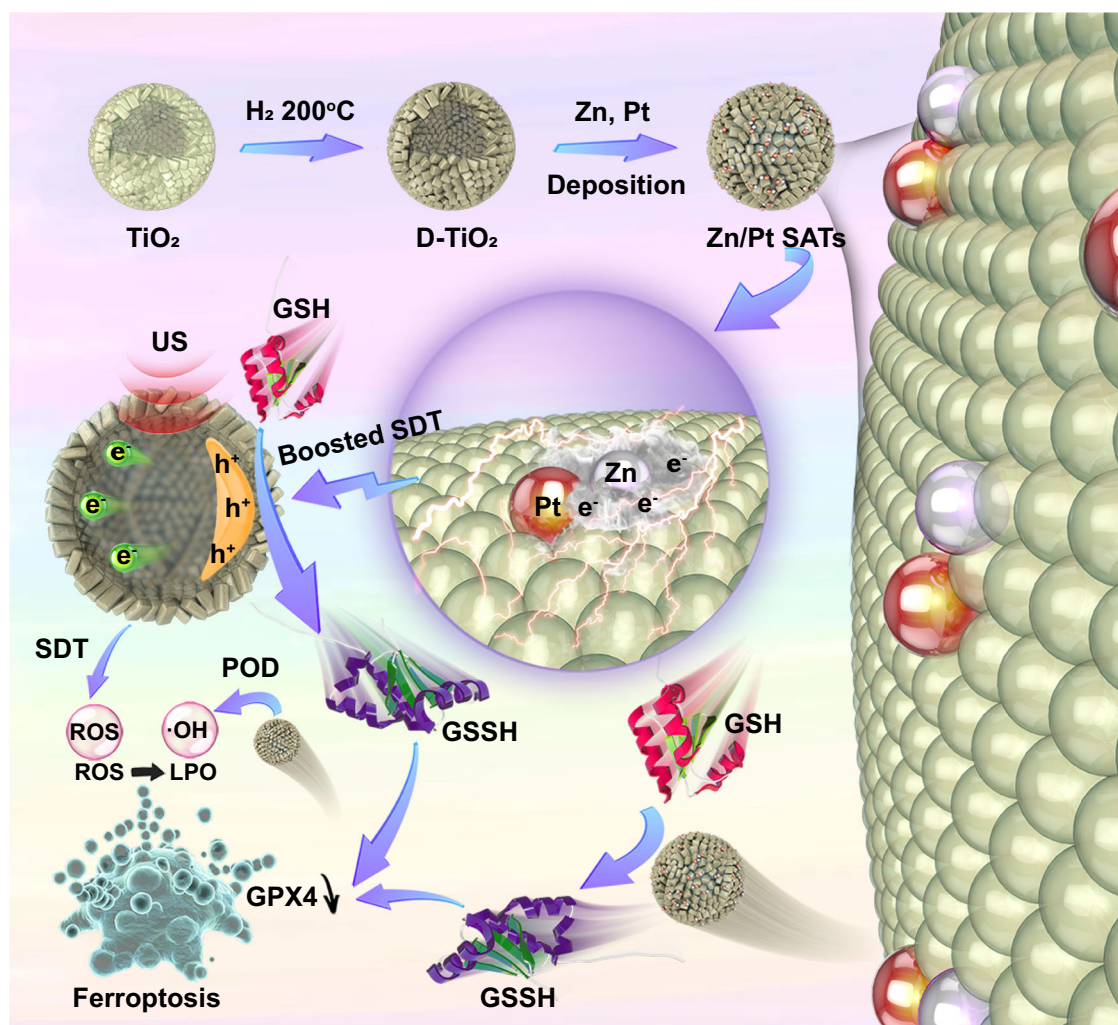


**Fig. 1** | Schematic illustration of Zn/Pt SATs sonosensitizer for cancer treatment.

## Results

### Synthesis and characterization of the high-performance Zn/Pt SATs

Firstly, TiO<sub>2</sub> nanospheres were treated in a reducing atmosphere to form D-TiO<sub>2</sub> with rich oxygen vacancies (Supplementary Fig. 1). As shown in Supplementary Fig. 2, the *g* value of D-TiO<sub>2</sub> is 2.004, which can be attributed to the oxygen vacancies consistent with the above result. Afterward, according to the reported method, Zn<sup>2+</sup> and Pt<sup>4+</sup> were introduced into the D-TiO<sub>2</sub> dispersion<sup>36</sup>. Subsequently, heat treatment was performed to stimulate the dual-site formation in Zn/Pt SATs. The transmission electron microscopy (TEM) images and elemental mappings of Zn/Pt SATs revealed Zn and Pt were homogeneously distributed over the whole D-TiO<sub>2</sub> nanospheres (Fig. 2a, b, d), wherein no particles were observed in Zn/Pt SATs. Furthermore, no Zn and Pt diffraction signals were exposed in X-ray diffraction (XRD) pattern of Zn/Pt SATs (Supplementary Fig. 3), which was consistent with the above results. Intuitively, the aberration-corrected high-angle annular dark-field scanning transmission electron microscopy (HAADF-STEM) image clearly displayed the bright dots revealed in pairs (Fig. 2c), which was consistent with the reported dual-site single-atom structure<sup>42</sup>. In addition, inductively coupled plasma-optical emission spectroscopy (ICP-OES) implies that the Zn and Pt contents in Zn/Pt SAT are 0.3 wt% and 1.0 wt%, respectively. That is, the molar ratio of Zn/Pt in Zn/Pt SAT is almost near 1:1, matching well with the dual-site single-atom structure. To demonstrate the superiority of the dual-site system in Zn/Pt SATs in the SDT process, Zn single-atom and Pt single-atom were anchored on D-TiO<sub>2</sub> supports nanospheres, respectively, as control samples through a similar method (named as Zn SATs and Pt SATs). No Zn or Pt diffraction peaks were exposed in the XRD patterns of Zn SATs or Pt SATs, manifesting the atomic dispersion status of Zn and Pt sites (Supplementary Fig. 3). Furthermore, the HAADF-STEM image shows several bright dots sprinkled on D-TiO<sub>2</sub> support, demonstrating that only isolated Zn and Pt atoms are existed on D-TiO<sub>2</sub> support, respectively (Supplementary Figs. 4 and 5). Subsequently, the Zeta potential difference between Zn/Pt SATs and D-TiO<sub>2</sub> also demonstrated the ingenious anchoring of Zn and Pt species (Supplementary Fig. 6). In contrast to D-TiO<sub>2</sub>, Zn/Pt SATs

presented a slight change in hydrodynamic size after Zn and Pt species were anchored on the D-TiO<sub>2</sub> support (Supplementary Fig. 7a). Additionally, Zn/Pt SATs could maintain good dispersity in water, PBS, and RPMI 1640 medium (Supplementary Fig. 7b), making them suitable for the physiological environment in vivo. Moreover, Zn/Pt SATs showed good colloidal stability (Supplementary Fig. 8).

### Zn/Pt dual-site single-atom precise coordination structure characterization of Zn/Pt SATs

To further investigate the chemical states and precise coordination environment of Zn and Pt in Zn/Pt SATs, synchrotron radiation-based characterizations are resorted. Firstly, as shown in Fig. 3a, the absorption energy position of Zn SATs and Zn/Pt SATs are close to that of ZnO, indicating that the oxidation state of Zn in Zn SATs and Zn/Pt SATs is similar to that in ZnO. Secondly, the coordination structure of Zn/Pt SATs is investigated by Fourier transform (FT) of extended X-ray absorption fine structure (EXAFS) spectra. As illustrated in Fig. 3b, FT of EXAFS curves of Zn/Pt SATs and Zn SATs show a dominant peak at 1.6 Å belonging to Zn–O bond, which is similar to that of ZnO (1.5 Å, Zn–O bond) and different from that of Zn foil (2.2 Å, Zn–Zn bond). Importantly, the strong peaks of Zn–O–Zn scattering path (2.9 Å) are absent in Zn/Pt SATs and Zn SATs, indicating the absence of ZnO clusters or nanoparticles. Specifically, Zn/Pt SATs exhibits a slightly higher peak at 2.8 Å than that of Zn SATs, which could be ascribed to Zn–O–Pt path. Thirdly, R space and k space fitting results of Zn in Zn/Pt SATs and Zn SATs are in good agreement with the original curves (Fig. 3c and Supplementary Figs. 9 and 10), and the coordination number of Zn with surrounding O atoms is 4.2 in Zn/Pt SATs (Supplementary Table 1), indicating that Zn atoms are connected with four O atoms, and the number of Zn–O–Pt scattering path is 0.8 (Supplementary Table 1). Moreover, compared with the wavelet transform (WT)-EXAFS (Fig. 3d) of Zn foil and ZnO references, it is found that the intensity maximum of Zn–Zn coordination (6.7 Å<sup>-1</sup>) and Zn–O–Zn scattering path (6.2 Å<sup>-1</sup>) are not observed in Zn/Pt SATs (4.5 Å<sup>-1</sup>). These results further corroborate the dominant presence of Zn–O–Pt species as evidenced by HAADF-STEM image. Similarly, the absorption edge of Pt SATs and Zn/Pt SATs are located between that of Pt foil and PtO<sub>2</sub>

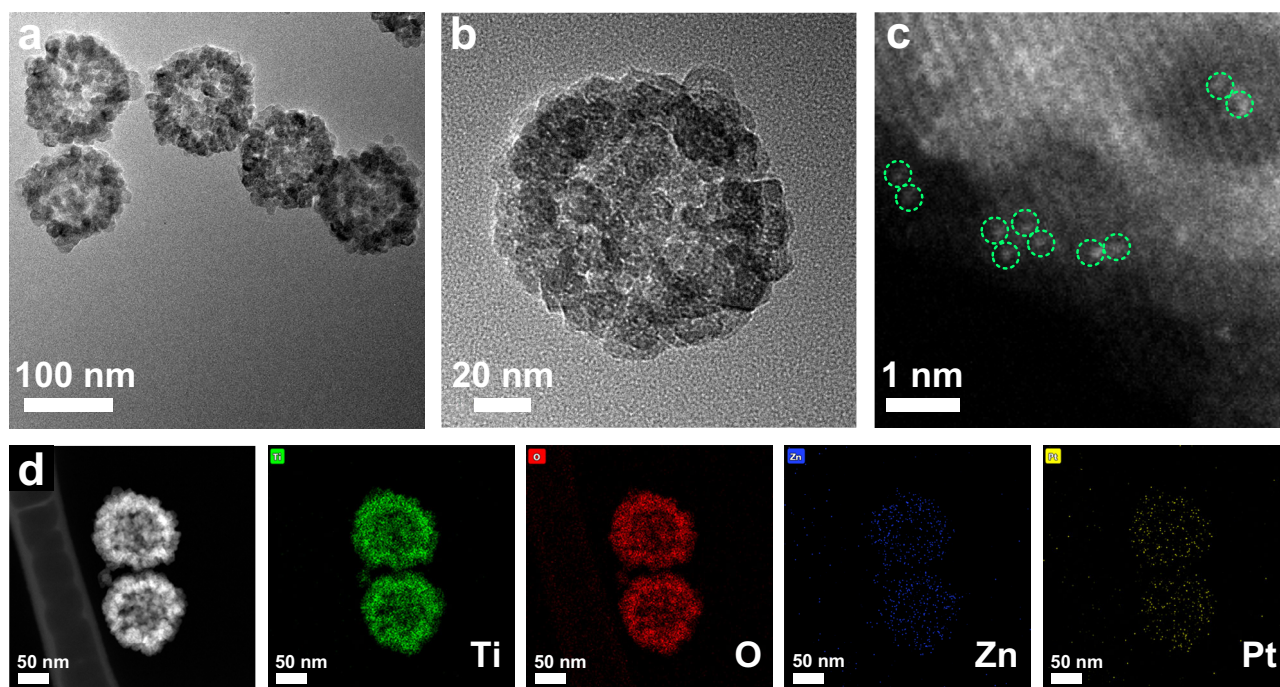


**Fig. 2 | Characterization of Zn/Pt SATs sonosensitizer.** a, b TEM images of Zn/Pt SATs. c HAADF-STEM image of Zn/Pt SATs. d Elemental mappings of Zn/Pt SATs. Representative results showed in a–d were obtained from three independent experiments. Source data are provided as a Source Data file.

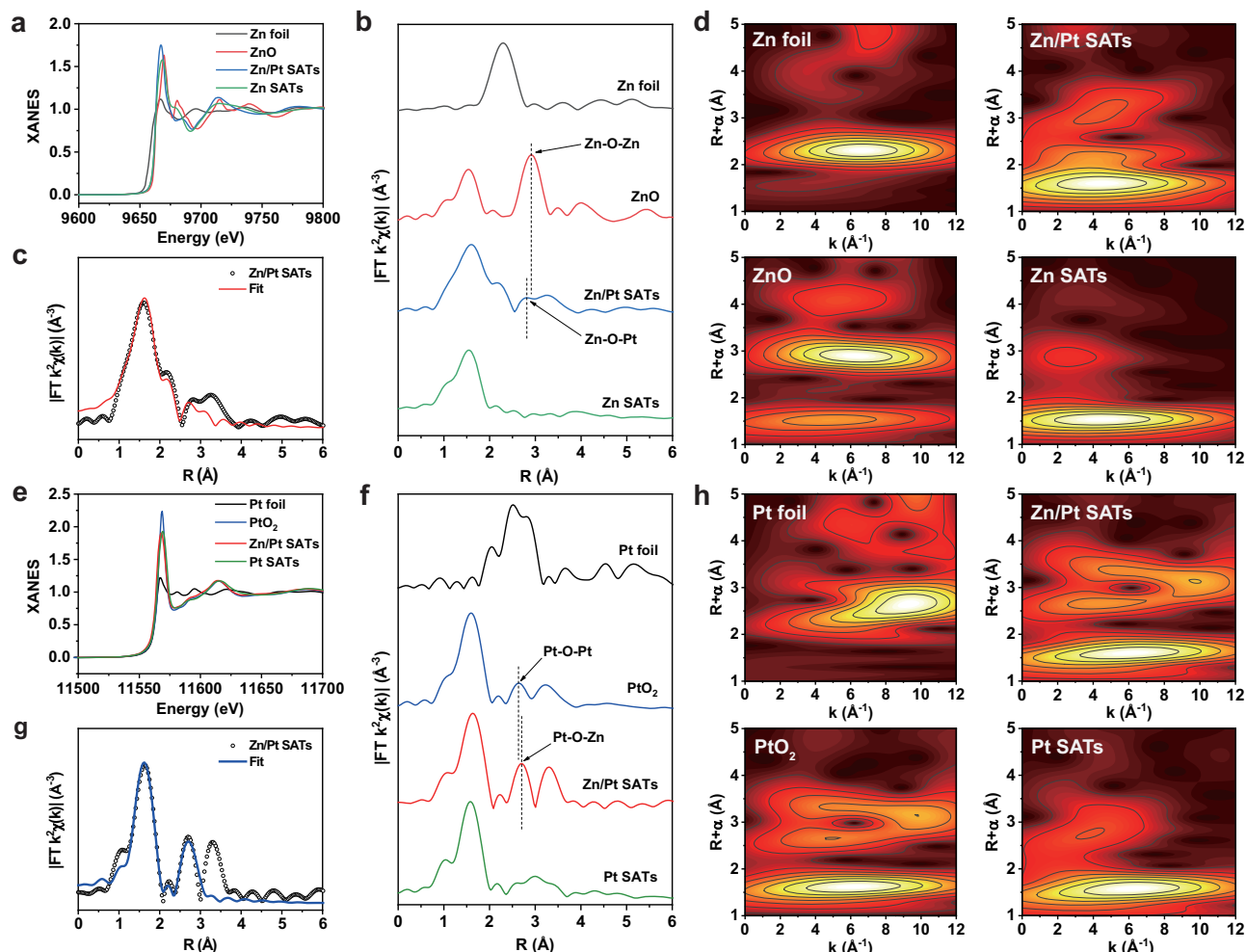


**Fig. 3 | Atomic structural analysis of Zn/Pt SATs sonosensitizer.** **a** Zn K-edge X-ray absorption near-edge structure (XANES) spectra of Zn SATs and Zn/Pt SATs. **b** Fourier transform magnitudes of Zn K-edge EXAFS spectra of Zn SATs and Zn/Pt SATs. **c** Zn EXAFS fitting result of Zn/Pt SATs in R space. **d** Wavelet transform EXAFS of Zn foil, ZnO, Zn/Pt SATs, and Zn SATs. **e** Pt L<sub>3</sub>-edge XANES spectra of Pt SATs and

Zn/Pt SATs. **f** Fourier transform magnitudes of Pt L<sub>3</sub>-edge EXAFS spectra of Pt SATs and Zn/Pt SATs. **g** Pt EXAFS fitting result of Zn/Pt SATs in R space. **h** Wavelet transform EXAFS of Pt foil, PtO<sub>2</sub>, Zn/Pt SATs, and Pt SATs. Source data are provided as a Source Data file.

(Fig. 3e), demonstrating that the chemical state of Pt is between 0 and +4 in Pt SATs and Zn/Pt SATs. In addition, the FT of Pt L<sub>3</sub>-edge EXAFS spectra in Zn/Pt SATs exhibits the peaks at  $R = 1.6 \text{ \AA}$  and  $2.8 \text{ \AA}$ , involving Pt–O and Pt–O–Zn scattering path (Fig. 3f). The R space and k space fitting results of Pt in Zn/Pt SATs and Pt SATs are in good agreement with the original curves (Fig. 3g and Supplementary Figs. 11 and 12), and the coordination number are 3.7 and 0.7 (Supplementary Table 2). The intensity maximum WT-EXAFS (Fig. 3h) of Zn/Pt SATs ( $6.2 \text{ \AA}^{-1}$ , Pt–O path;  $9.8 \text{ \AA}^{-1}$ , Pt–O–Zn path) is different from that of Pt foil ( $9.3 \text{ \AA}^{-1}$ , Pt–Pt path) and Pt SATs ( $6.2 \text{ \AA}^{-1}$ , Pt–O path). It should be noted that the peak at  $9.8 \text{ \AA}^{-1}$  may be attributed to the second coordination (Zn/Pt SATs, Pt–O–Zn path; PtO<sub>2</sub>, Pt–O–Pt path). In brief, it is verified the presence of Zn–O–Pt structure in Zn/Pt SATs is consistent with the HAADF-STEM image result.

### ROS regulation of Zn/Pt SATs

The integration of dual-site structure and D-TiO<sub>2</sub> endowed Zn/Pt SATs enhanced ROS production capacity during SDT. As illustrated in Fig. 4a, the Zn/Pt SATs exhibit the highest <sup>1</sup>O<sub>2</sub> yield compared with traditional D-TiO<sub>2</sub>, Zn SATs, and Pt SATs under the same US condition. Besides, the Zn SATs and Pt SATs were indeed superior to traditional D-TiO<sub>2</sub>. The results identified that SDT outcome could be significantly promoted by the formation of Zn and Pt dual-single-atom structures in

Zn/Pt SATs. In detail, with the anchoring of Zn and Pt dual atoms, Zn/Pt SATs could produce more <sup>1</sup>O<sub>2</sub> under US irradiation compared with Zn SATs and Pt SATs, identifying that only a single Zn site or Pt site was not sufficient to produce the desired enhancement effect of SDT and Zn/Pt dual-single-atom structure was superior to Zn or Pt single-atom structure. Moreover, Zn/Pt SATs with CAT-like activity could provide abundant oxygen (O<sub>2</sub>) from H<sub>2</sub>O<sub>2</sub> solution (Supplementary Fig. 13). As shown in Fig. 4b, c, the <sup>1</sup>O<sub>2</sub> production of Zn/Pt SATs increases significantly in the presence of H<sub>2</sub>O<sub>2</sub> under US irradiation, which is attributed to the CAT-like activity of Zn/Pt SATs that can catalyze H<sub>2</sub>O<sub>2</sub> to produce O<sub>2</sub> and further promote the production of <sup>1</sup>O<sub>2</sub>. Additionally, <sup>1</sup>O<sub>2</sub> production behaved power density dependence in the presence of Zn/Pt SATs under US irradiation (Fig. 4d). Successively, the ·OH generation ability of Zn/Pt SATs was studied. As expected, Fig. 4e shows the same tendency as Fig. 4a, Zn/Pt SATs exhibited the most ·OH yield compared with Zn SATs, Pt SATs, and D-TiO<sub>2</sub> under US irradiation, demonstrating the superiority of Zn/Pt dual-site structure during SDT. Based on the above results, we speculated that the synergistic effect of neighboring Zn/Pt dual-atom could enhance the SDT effect of Zn/Pt SATs. Subsequently, we investigated the POD-like activity of Zn/Pt SATs in mimic mildly acidic tumor microenvironment TME (pH 6.5). The ·OH production could oxidize 3,3',5,5'-tetramethylbenzidine (TMB) to oxidized TMB (oxTMB). As illustrated in

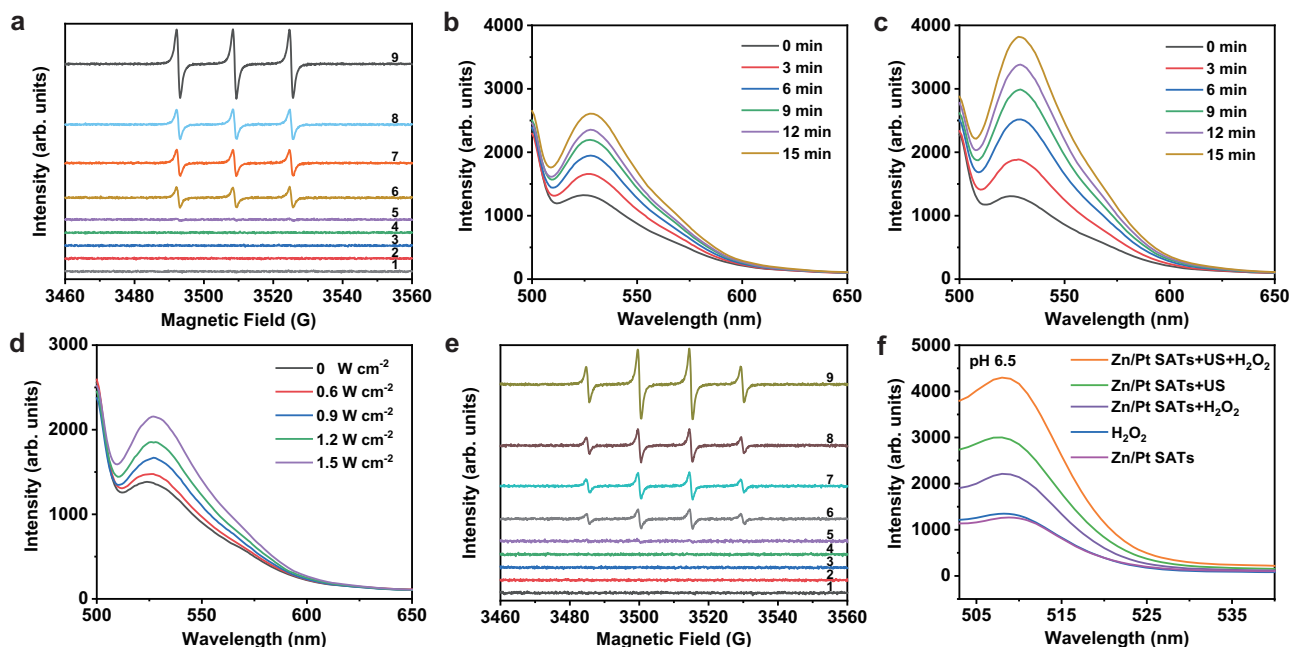


**Fig. 4 | ROS regulation by Zn/Pt SATs.** **a** Comparison of  $^1\text{O}_2$  generation quantified by ESR spectra of TEMP/ $\text{O}_2$  for different groups of (1) D-TiO<sub>2</sub>, (2) Zn SATs, (3) Pt SATs, (4) Zn/Pt SATs, (5) US, (6) D-TiO<sub>2</sub> + US, (7) Zn SATs+US, (8) Pt SATs+US, and (9) Zn/Pt SATs+US. **b** Time-dependent fluorescence intensity changes of SOSG probe in the presence of Zn/Pt SATs under US irradiation. **c** Time-dependent fluorescence intensity changes of SOSG probe in the presence of Zn/Pt SATs and H<sub>2</sub>O<sub>2</sub> under US irradiation. **d** Power density-dependent fluorescence intensity

changes of SOSG probe in the presence of Zn/Pt SATs under US irradiation. **e** Comparison of  $\cdot\text{OH}$  generation quantified by ESR spectra of DMPO/ $\cdot\text{OH}$  for different groups of (1) D-TiO<sub>2</sub>, (2) Zn SATs, (3) Pt SATs, (4) Zn/Pt SATs, (5) US, (6) D-TiO<sub>2</sub> + US, (7) Zn SATs+US, (8) Pt SATs+US, and (9) Zn/Pt SATs+US. **f** Comparison of  $\cdot\text{OH}$  generation of Zn/Pt SATs with different treatments quantified by fluorescence intensity changes of HPF. Source data are provided as a Source Data file.

Supplementary Fig. 14, the absorption peaks of oxTMB increased with time in the presence of Zn/Pt SATs, TMB, and H<sub>2</sub>O<sub>2</sub>. The maximal reaction velocity ( $V_{\text{max}}$ ) and Michaelis–Menten constant ( $K_{\text{m}}$ ) of Zn/Pt SATs were  $1.87 \times 10^{-7} \text{ Ms}^{-1}$  and 1.65 mM, respectively (Supplementary Fig. 15). Thereupon, we explored the  $\cdot\text{OH}$  generated from SDT and POD-like activity in mimic acidic TME (pH 6.5). The result shows that Zn/Pt SATs with POD-like activity could enrich  $\cdot\text{OH}$  production pathways during SDT in mimic acidic TME and make Zn/Pt SATs possess great potential in antitumor therapy (Fig. 4f). Furthermore, 5,5'-dithiobis-(2-nitrobenzoic acid) (DTNB) was used to evaluate the depletion of GSH. Supplementary Fig. 16 shows the significant decrease in the absorbance of DTNB over time, which is indicative of GSH depletion by Zn/Pt SATs. This reduced the ROS clearance effect of overexpressed GSH in tumor, which is beneficial for ROS-sensitive antitumor therapy.

### DFT theoretical simulations

To understand the physical mechanisms of ROS production by Zn/Pt SATs under US stimuli, the theoretical calculation can be an effective method to reveal the sonodynamic process. Since the excitation process is a dynamic process, the electronic structure (density of state (DOS) and energy levels) was employed to analyze the reaction. The structural information, total DOS (TDOS), and partial DOS (PDOS) of pure TiO<sub>2</sub>, Zn SATs, Pt SATs, and Zn/Pt SATs are shown in Supplementary Table 3, Supplementary Table 4, Supplementary Fig. 17 and Fig. 5, respectively. The valence band state of pure TiO<sub>2</sub> is near the fermi level, indicating that it belongs to P-type semiconductor, i.e. the charge carrier is hole as energy excitation occurred (Supplementary Fig. 17a). For Zn SATs and Pt SATs, the fermi level moves to conductive band, especially the fermi level of Zn SATs moves closely to the bottom of conductive band (Supplementary Fig. 17b, c). This indicates that the anchored Zn and Pt atoms can improve the conductivity of TiO<sub>2</sub>, while TiO<sub>2</sub> tends to transfer from P-type to N-type semiconductors for Zn

SATs. For PDOS (Fig. 5a), it can be seen that the valance and conductive bands of TiO<sub>2</sub> are mainly constituted by the O-2p and Ti-3d orbital, respectively. The introduced Zn can indirectly influence the energies of valance and conductive band referenced to the fermi level (Fig. 5b). However, for the introduced Pt, the impurity band in the band gap consisting of the Pt-5d orbital could be found, which can directly reduce the band gap and electron transfer energy (Fig. 5c). Thus, it can be concluded that Zn could improve the electronic conduction and Pt can lower the band gap by the impurity band. For Zn-Pt co-adsorption configuration (Supplementary Fig. 17d and Fig. 5d), both the conductivity and band gap are improved, therefore, Zn and Pt are co-assisted the electron excitation in TiO<sub>2</sub>. Meanwhile, for  $^3\text{O}_2$  adsorption, Zn/Pt SATs are more favorable (The adhesion energy of  $-1.35 \text{ eV}$ , O-O bond of  $1.383 \text{ \AA}$ ) than those of Zn ( $-0.54 \text{ eV}$ , O-O bond of  $1.290 \text{ \AA}$ ) and Pt SATs ( $-0.57 \text{ eV}$ , O-O bond of  $1.291 \text{ \AA}$ ). The PDOS and COHP of  $^3\text{O}_2$  adsorption are concluded in Supplementary Fig. 18. For  $^3\text{O}_2$  adsorption on Zn SATs, the anti-bonding state of  $^3\text{O}_2$  will interact with the Zn atom near the Fermi level, and will be partially occupied (Supplementary Fig. 18a) with the ICOHP of  $-7.43/-8.47$  in spin up/down channel for O-O bond (Supplementary Fig. 18b, c). A similar trend could also be found for Pt SATs (Supplementary Fig. 18d), in which the Pt-5d orbital will mainly interact with the anti-bonding state of  $^3\text{O}_2$  with ICOHP of  $-6.03/-8.12$  in spin up/down channel for O-O bond (Supplementary Fig. 18e, f). This suggests that both Pt and Zn can interact with  $^3\text{O}_2$ , while the Pt seems more favorable and effective. Interestingly, for Zn/Pt SATs, the Pt-5d orbital distinctly interacts with the anti-bonding state of  $^3\text{O}_2$  below the fermi level (Supplementary Fig. 18g), indicating that such an anti-bonding state could be occupied by the electron and  $^3\text{O}_2$  can be effectively activated with weaker O-O bond (ICOHP of  $-6.04/-7.51$  in spin up/down channel, Supplementary Fig. 18h, i), compared with the ICOHP of  $-6.47/-9.80$  in spin up/down channel for pure  $^3\text{O}_2$  molecule (Supplementary Fig. 19). The weakened O-O bond in the adsorption state can also be supported by the differential charge

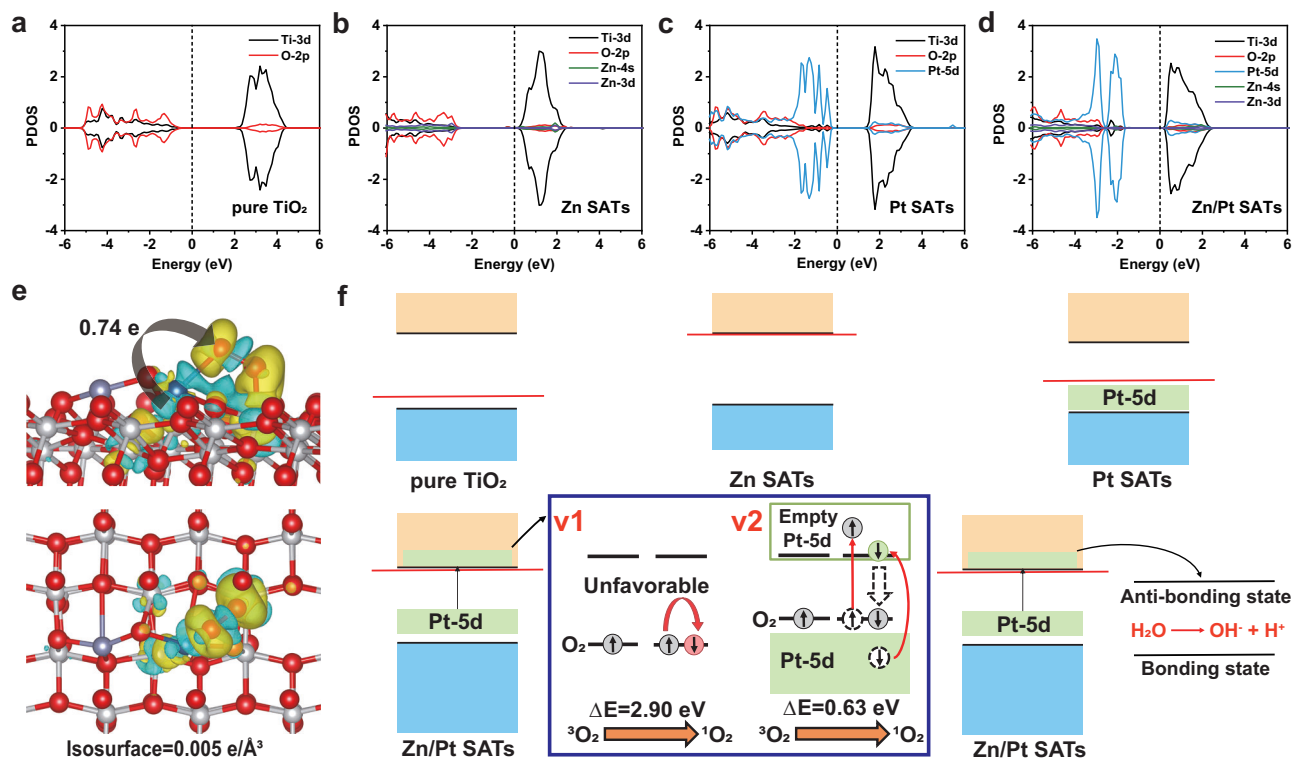


**Fig. 5 | Density functional theory (DFT) calculations.** **a–d** The partial density of state (PDOS) of pure TiO<sub>2</sub>, Zn SATs, Pt SATs, and Zn/Pt SATs, respectively. **e** The differential charge for O<sub>2</sub> adsorption on Zn/Pt SATs, the top- and side-view for the top and bottom illustration, respectively. The isosurface is 0.005 e/Å<sup>3</sup>, while the

yellow and blue denote the electron accumulation and deficiency, respectively. **f** The concluded mechanisms of Zn/Pt SATs for activating O<sub>2</sub> and H<sub>2</sub>O. Source data are provided as a Source Data file.

(Fig. 5e), the electron will be transferred from Pt in Zn/Pt SATs to adsorbed <sup>3</sup>O<sub>2</sub> and lower the interaction of O–O bond.

Such an effect makes the transition of <sup>3</sup>O<sub>2</sub> to <sup>1</sup>O<sub>2</sub> possible. Based on the electronic structure change for <sup>3</sup>O<sub>2</sub> and <sup>1</sup>O<sub>2</sub> adsorbed on Zn/Pt SATs (Supplementary Fig. 20), the mechanism of Zn/Pt SATs promotes the production of <sup>1</sup>O<sub>2</sub>. For adsorbed <sup>3</sup>O<sub>2</sub> and <sup>1</sup>O<sub>2</sub> (Supplementary Fig. 20), the PDOS shows that the occupied 2p orbital (–1 eV) in the spin-up channel of <sup>3</sup>O<sub>2</sub> will move above the fermi level in <sup>1</sup>O<sub>2</sub> (Supplementary Fig. 20a). This suggests that the electron in such occupied 2p orbital (spin up) of <sup>3</sup>O<sub>2</sub> is lost. On the contrary, the empty 2p orbital (spin down) in <sup>3</sup>O<sub>2</sub> will be moved below the fermi level in <sup>1</sup>O<sub>2</sub> (Supplementary Fig. 20b), suggesting the empty 2p orbital in the spin-down channel will obtain an electron. Since the direct change state of the electronic spin state in O<sub>2</sub> is impossible due to the high energy of 2.90 eV (Fig. 5f, v1). Therefore, we can deduce that the electron transition of Zn/Pt SATs will improve the spin state change of electrons in the adsorbed <sup>3</sup>O<sub>2</sub>. Under the action of the external field (US), the electron in the spin-up channel in adsorbed <sup>3</sup>O<sub>2</sub> may move into the empty Pt-5d orbital (Supplementary Fig. 20c), meanwhile, the electron in the spin-down channel of the occupied Pt-5d orbital can be inspired by the external field to the empty 2p orbital with the same spin state in <sup>3</sup>O<sub>2</sub> (Supplementary Fig. 20d). Following that, the spin down 2p orbital of O atom obtained electron will move below the fermi level to form the <sup>1</sup>O<sub>2</sub> (Fig. 5f, v2). Overall, the Pt-based catalyst can act as the electronic acceptor and donor to achieve the transition of the electronic spin state in <sup>3</sup>O<sub>2</sub> (Fig. 5f, v2). Based on supposed the mechanism, it is seen that the electronic structure and the electron transfer are two important factors. Since the contribution of Zn-3d is negligible near the fermi level, only the Pt SATs and Zn/Pt SATs will be employed to show the difference in <sup>1</sup>O<sub>2</sub> production. For <sup>3</sup>O<sub>2</sub> adsorbed on Pt SATs (Supplementary Fig. 21), the <sup>3</sup>O<sub>2</sub> states will cover the gap near the fermi level in spin up channel, suggesting that the electron can be easily

transferred from <sup>3</sup>O<sub>2</sub> to empty Pt-5d orbital (Supplementary Fig. 21a, b for adsorbed <sup>3</sup>O<sub>2</sub> and Supplementary Fig. 21d, e for adsorbed <sup>1</sup>O<sub>2</sub>). However, for the spin-down channel (Supplementary Fig. 21c for adsorbed <sup>3</sup>O<sub>2</sub> and Supplementary Fig. 21f for adsorbed <sup>1</sup>O<sub>2</sub>), the first peak at –1 eV below the fermi level in adsorbed <sup>3</sup>O<sub>2</sub> is the interaction of Pt–O (Supplementary Fig. 21g–i), which cannot provide electron to keep the adsorption state. Thus, the peak near the –1.98 eV in the spin-down channel is the main 5d orbital of electronic donor (Supplementary Fig. 21g). It is farther from the fermi level than that of Zn/Pt SATs (–1.52 eV), indicating that the electron transfer to <sup>3</sup>O<sub>2</sub> empty orbital in spin-down channel is unfavorable. Therefore, in addition to impurity band of Pt-5d, the high electron conduction property caused by Zn loading is also very important. The energy change of <sup>3</sup>O<sub>2</sub>→<sup>1</sup>O<sub>2</sub> with gas phase, adsorption on Pt SATs and Zn/Pt SATs are 2.90 eV, 0.84 eV, and 0.64 eV (Supplementary Fig. 22), respectively, which also proves the conclusion. In addition, Zn and Pt are co-assisted the electron transferred can also improve H<sub>2</sub>O activation. For adsorbed H<sub>2</sub>O, the location of anti-bonding state of H<sub>2</sub>O is close to that of the conductive band of Zn/Pt SATs (Supplementary Fig. 23). In addition, the sustained sonodynamic process could provide enough energy to make the weakened O–H dissociate.

### Intracellular SDT of Zn/Pt SATs

Encouraged by the excellent sonodynamic performance of Zn/Pt SATs, the therapeutic effect of Zn/Pt SATs at the cellular level was assessed. Initially, the cytotoxicity of Zn/Pt SATs was investigated via two cell lines by cell counting kit 8 (CCK-8) assay. As shown in Supplementary Fig. 24, no obvious cytotoxicity was exhibited on L929 cells, identifying the preminent biocompatibility of Zn/Pt SATs. In contrast, Zn/Pt SATs presented a certain cell-killing effect on 4T1 cells, which is attributed to the production of ·OH resulting from the POD-like activity of Zn/Pt SATs (Fig. 6a)<sup>43</sup>. Excitingly, Zn/Pt SATs (400 μg mL<sup>–1</sup>) exhibit a

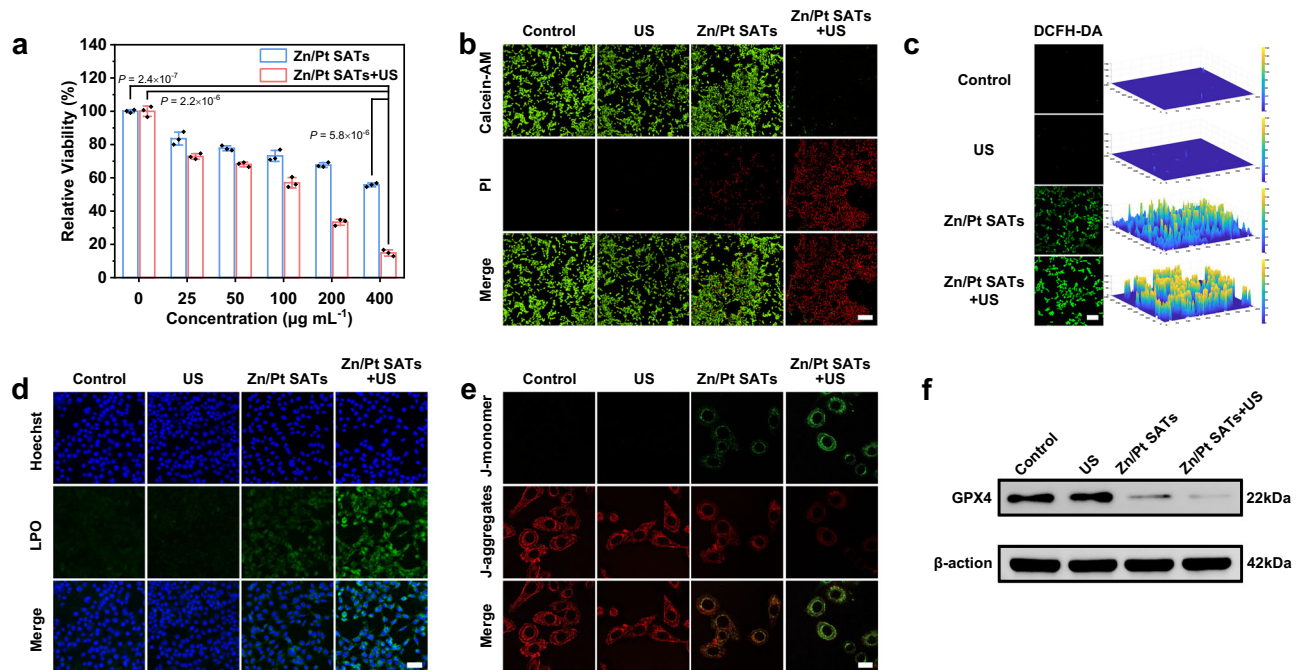


**Fig. 6 | In vivo SDT efficiency assessments.** **a** Cytotoxicity of 4T1 cells after treatment with Zn/Pt SATs or Zn/Pt SATs+US (Mean  $\pm$  S.D.,  $n = 3$  independent experiments), a two-tailed  $t$  test was used to calculate  $P$  values. **b** Confocal images of 4T1 cells stained with Calcein-AM and PI after different treatments. (scale bar: 200  $\mu\text{m}$ ). **c** Confocal images of 4T1 cells stained with DCFH-DA after different treatments. (scale bar: 100  $\mu\text{m}$ ). **d** Confocal images of LPO detection of 4T1 cells

(scale bar: 50  $\mu\text{m}$ ). **e** Confocal images of 4T1 cells detected with JC-1 assay kit after different treatments (scale bar: 20  $\mu\text{m}$ ). **f** Western blot analysis of GPX4 expression after different treatments. Representative results showed in **b–f** were obtained from three independent experiments. Source data are provided as a Source Data file.

satisfactory 4T1 cell death effect with the further addition of US irradiation. Additionally, the cell-killing ability of Zn/Pt SATs was further visually displayed via live/dead cell staining analysis (Fig. 6b). Subsequently, the flow cytometry analysis precisely manifested the cell-killing effect of Zn/Pt SATs under US irradiation, which was similar to the above experiment results (Supplementary Fig. 25). Afterward, the possible mechanism of ROS generation was studied by 2',7'-dichlorodihydrofluorescein diacetate (DCFH-DA). As displayed in Fig. 6c, weak green fluorescence in control and US groups and distinct green fluorescence in Zn/Pt SATs and Zn/Pt SATs+US groups could be detected. In particular, the Zn/Pt SATs+US group behaves with a stronger fluorescence intensity than the Zn/Pt SATs group, indicating the surge of intracellular ROS.

As expected, the Zn/Pt SATs+US group shows significant up-regulation of LPO compared with Zn/Pt SATs group (Fig. 6d), indicating that SDT process produces more ROS that contributes to the further accumulation of LPO and enhances ferroptosis. The decrease or disappearance of the mitochondrial ridge (Supplementary Fig. 26), and the decrease of mitochondrial membrane potential (Fig. 6e), suggest the ferroptosis<sup>44</sup>. Moreover, the intracellular GSH was reduced after incubating with Zn/Pt SATs. In Zn/Pt SATs+US group, the intracellular GSH was depleted dramatically, indicating GSH was further consumed by the oxidation of GSH to GSSG via sonoexcited holes (Supplementary Fig. 27)<sup>45</sup>. Subsequently, the down-regulation of GPX4 protein manifested the realization of SDT in Zn/Pt SATs+US group could significantly silence GPX4 protein compared with Zn/Pt SATs group (Fig. 6f). It is suggested that US irradiation could enable Zn/Pt SATs to enhance ferroptosis of cancer cells.

### In vivo oncotherapy of Zn/Pt SATs

Benefiting from the desirable properties of Zn/Pt SATs, we subsequently studied its antitumor effect on tumor-bearing mice. Prior to oncotherapy, we explored the biodistribution of Zn/Pt SATs in major

organs and tumor tissue by inductively coupled plasma mass spectrometry (ICP-MS) to determine the optimal window for treatment (Supplementary Fig. 28). It could be seen that Zn/Pt SATs enriched at tumor site and achieved maximum accumulation around 24 h after intravenous injection. Thereupon, the treatment was performed after 24 h of intravenous injection (Fig. 7a). Briefly, when the tumor volume was about 100 mm<sup>3</sup> in volume, the tumor-bearing mice were randomly divided into four groups ( $n = 5$ ): (1) control, (2) US, (3) Zn/Pt SATs, and (4) Zn/Pt SATs+US. After intravenous injection of Zn/Pt SATs for 24 h, US irradiation (1.5 W cm<sup>-2</sup>, 5 min, 1.0 MHz, 50% duty cycle) was performed in (2) and (4) groups. During the treatment, the weight of the mice and the volume of the tumors were monitored every two days. The difference in body weight changes among the groups was within the margin of error (Fig. 7b), indicating the adverse effects of various treatments on the body function of mice could be ignored. Furthermore, no obvious damages were exposed in H&E staining of the major organ tissues treated by various treatments (Supplementary Fig. 29), suggesting the superior biosafety of Zn/Pt SATs. Combined with tumor growth curves, excised tumor weights, and photographs of excised tumors, Zn/Pt SATs+US group demonstrated an excellent tumor suppression effect (Fig. 7c–e and Supplementary Fig. 30). Subsequently, the immunofluorescence staining in Zn/Pt SATs+US group shows the further down-regulation of GPX4 compare with Zn/Pt SATs group, identifying that the presence of SDT contributes to the enhancement of ferroptosis (Fig. 7f). In addition, the terminal deoxynucleotidyl transferase-mediated dUTP nick end labeling (TUNEL) staining, and hematoxylin and eosin (H&E) staining demonstrated severe cell apoptosis in Zn/Pt SATs+US group (Fig. 7g, h), confirming tumor growth was inhibited by SDT and ferroptosis effectively. Furthermore, a desirable survival rate was shown after Zn/Pt SATs+US treatment (Supplementary Fig. 31). Overall, these above results strongly manifested that dual-site single-atom synergistic-augmented SDT combined with SDT-boosted

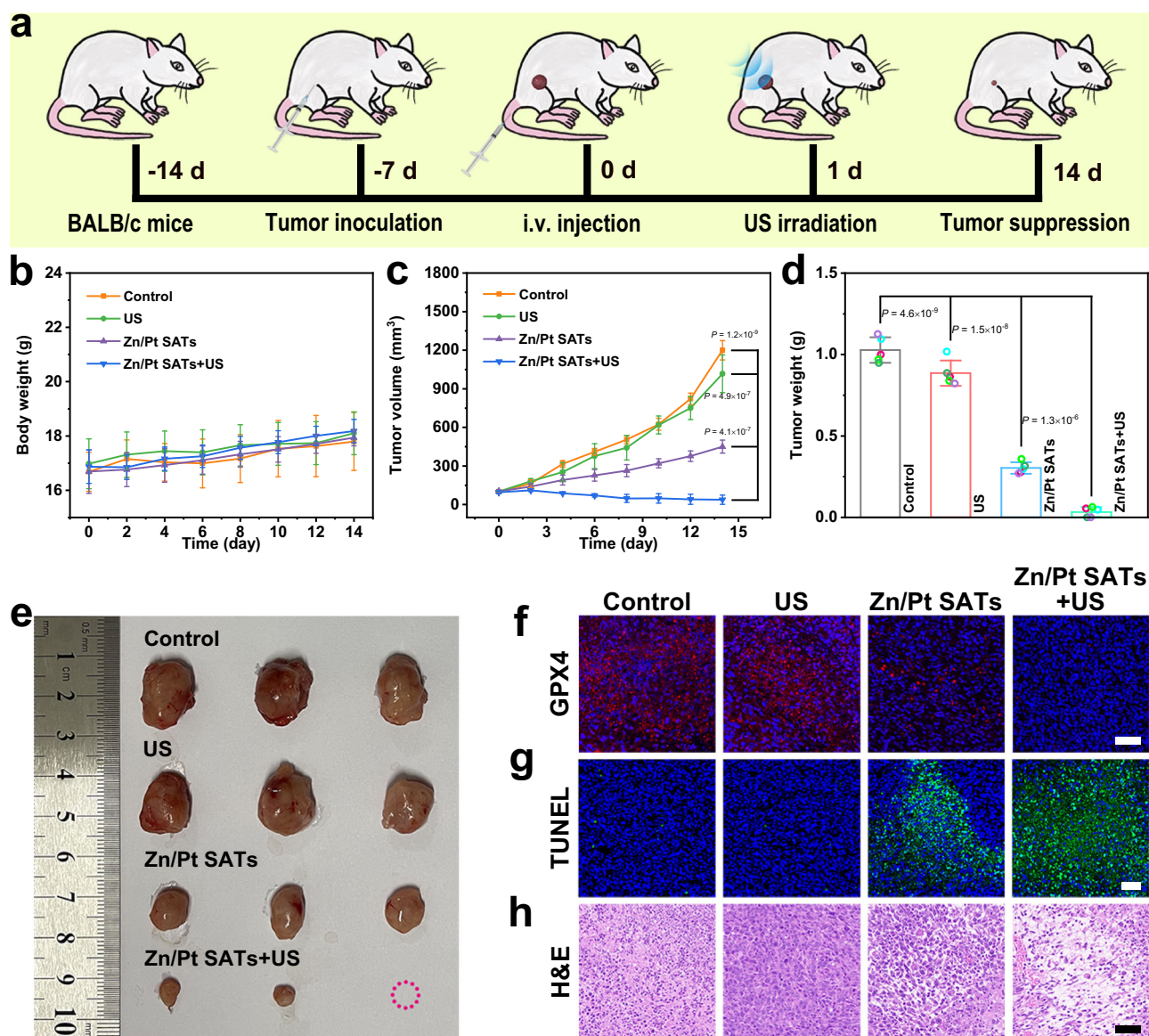


**Fig. 7 | In vivo oncotherapy efficiency assessments.** **a** Therapeutic procedure for 4T1 tumor-bearing mice. **b** Body weight curves after various treatments (Mean  $\pm$  S.D.,  $n = 5$  mice). **c** Tumor growth curves of mice after various treatments (Mean  $\pm$  S.D.,  $n = 5$  mice), a two-tailed  $t$  test was used to calculate  $P$  values. **d** Average tumor weights of mice at 14 day post various treatments (Mean  $\pm$  S.D.,  $n = 5$  mice), a two-tailed  $t$  test was used to calculate  $P$  values. **e** Representative photographs of

excised tumors. **f** GPX4 staining of tumor slices after various treatments (scale bar: 50  $\mu$ m). **g** TUNEL staining of tumor slices after various treatments (scale bar: 50  $\mu$ m). **h** H&E staining of tumor slices from different groups after various treatments (scale bar: 50  $\mu$ m). Representative results showed in **f–h** were obtained from three independent experiments. Source data are provided as a Source Data file.

ferroptosis can achieve excellent antitumor effect without obvious long-term toxicity concerns.

## Discussion

In summary, we built a dual-site single-atom driven difunctional superimposition-augmented sonosensitizer for SDT and sono-boostered ferroptosis, which can effectively suppress tumor growth. The characteristic dual-site structure of Zn/Pt SATs sonosensitizer greatly promotes ROS yield during SDT. It is worth noting that Zn single-atoms and Pt single-atoms play two different roles in assisting electron excitation of Zn/Pt SATs. The DFT calculation demonstrates that Zn and Pt atoms could improve the electron conductivity and excitation efficiency under US irradiation respectively, which means this process can extremely augment the separation efficiency of electrons and holes and yield of ROS. Both experiments and DFT calculations prove Zn/Pt dual-site single-atom driven difunctional superimposition-

augmented effect is better than Zn single-atom or Pt single-atom driven augmented effect.

Additionally, the intrinsic GSH degradation capacity and POD-like activity of Zn/Pt SATs can down-regulate GPX4 expression and LPO accumulation to induce ferroptosis. Under US stimuli, the sonoexcited holes and the rapid increase of extra ROS during SDT process could further boost ferroptosis. Moreover, the accumulation of ROS by Zn/Pt SATs is beneficial for tumor necrosis. Consequently, the Zn/Pt SATs +US group exhibits better tumor cell-killing effect than Zn/Pt SATs group at cell level. As expected, the Zn/Pt SATs sonosensitizer shows satisfactory in vivo oncotherapy effect under US irradiation.

This finding innovatively verifies the regulation effect of dual single-atom structure on SDT, which sheds substantial light on the development of dual single-atom sonosensitizer and proposes a hopeful direction for improving the SDT efficacy and ferroptosis of tumor.



## Methods

### Cell lines and mice

4T1 cell line (Catalog no. CRL-2539) and L929 cell line (Catalog no. CCL-1) were purchased from and authenticated by ATCC. The test results for Mycoplasma contamination in these cell lines were stated to be negative by the supplier. All cell lines in this work are not listed by the International Cell Line Authentication Committee as cross-contaminated or misidentified cell lines (v12, 2023).

A total of 110 healthy female BALB/c mice (~six weeks old) needed for the experiment were purchased from the Center for Experimental Animals, Jilin University (Changchun, China). The handling procedures were in compliance with the guidelines of the Institutional Animal Care and Use Committee of Changchun Institute of Applied Chemistry, Chinese Academy of Sciences (Grant no. 20220001) (the maximal tumor burden permitted was 2000 mm<sup>3</sup>). All mice were maintained at 12-h light-dark cycle within 23–27 °C and 40–55% humidity. There was no tumor burden exceeding the maximum tumor burden permitted by the institutional review board. A tumor mouse model was established by hypodermic injection of 4T1 cells into the right leg of each mouse.

### Materials

Polyvinylpyrrolidone (PVP, Mw ~40,000), titanium (IV) fluoride, and zinc chloride (99.99%) were purchased from Sigma-Aldrich. Chloroplatinic acid hexahydrate and Ammonium carbonate ((NH<sub>4</sub>)<sub>2</sub>CO<sub>3</sub>, ≥99%) were purchased from Aladdin. Hydrochloric acid (HCl, AR) and ethanol (AR) were purchased from Beijing Chemical Works. All the reagents were used as received without any further purification.

### Characterizations

TEM images were obtained with a FEI TECNAI G2 high-resolution TEM. The HAADF-STEM images were obtained with a Titan 80–300 scanning/TEM. Powder XRD patterns were obtained on a D8 ADVANCE X-ray diffractometer. ICP-MS measurements were performed on an ELAN 9000/DRC. ICP-OES measurements were taken on a PerkinElmer ICP instrument. The absorption spectrum was recorded on Shimadzu UV-3600 spectrophotometer. Electron paramagnetic resonance (EPR) spectra and electron spin resonance (ESR) spectra were taken on a Bruker A300. Hydrodynamic size and Zeta potential were measured by using a Malvern instrument Zetasizer Nano system.

### Synthesis of TiO<sub>2</sub> nanospheres

TiF<sub>4</sub> aqueous solution (0.04 M, 2.5 mL), polyvinylpyrrolidone aqueous solution (9.75 mg mL<sup>-1</sup>, 4 mL), ethanol (27.6 mL), and HCl (0.1 M, 250 μL) were mixed. The mixture was aged at room temperature for 1 h. Then, the mixture was poured into a stainless-steel autoclave and kept it at 180 °C for 3 h. Ultimately, TiO<sub>2</sub> nanospheres were purified via centrifugation and subjected to multiple washing cycles.

### Synthesis of D-TiO<sub>2</sub> nanospheres

TiO<sub>2</sub> nanospheres were transferred to a tube furnace and treated with 5% H<sub>2</sub>/Ar atmosphere at 200 °C for 4 h to obtain D-TiO<sub>2</sub> nanospheres. The temperature was achieved at a ramp rate of 5 °C/min from room temperature.

### Synthesis of Zn/Pt SATs

D-TiO<sub>2</sub> nanospheres (500 mg) were dispersed into 30 mL of water. After stirring for 15 min, the dispersion was properly alkaline by adding ammonium carbonate. ZnCl<sub>2</sub> (3.5 mg) and H<sub>2</sub>PtCl<sub>6</sub>·6H<sub>2</sub>O (20 mg) dissolved in 15 mL of water were introduced into the D-TiO<sub>2</sub> dispersion dropwise (about one drop per second). The mixture was aged at room temperature for 1 h, then treated by 5% H<sub>2</sub>/Ar atmosphere at 160 °C for 1 h. The temperature was achieved at a ramp rate of 2 °C/min from room temperature. The Zn SATs and Pt SATs were synthesized through the same method based on D-TiO<sub>2</sub>, which only loaded with the same amount of Zn or Pt as Zn/Pt SATs on D-TiO<sub>2</sub> supports.

### Sample preparation of ICP-MS and ICP-OES measurements

5 mL of HNO<sub>3</sub>, 3 mL of HCl, 1 mL of HF, and 2 mL of H<sub>2</sub>O<sub>2</sub> were added to the sample. Then, the mixture was transferred to a sealed PTFE container and put it into a microwave digestion furnace. The mixture was treated at 130 °C for 5 min and then heated to 180 °C for 40 min. After the mixture was cooled at room temperature, it was diluted to the mark with deionized water. Finally, the content of various elements in the sample was detected via ICP-MS and ICP-OES.

### XAFS measurements

Specifically, the X-ray absorption fine structure spectra of Zn K-edge and Pt L<sub>3</sub>-edge were obtained at 44 Å beamline of National Synchrotron Radiation Research Center (NSRRC) Taiwan and monochromatized with Si(111) double-crystal<sup>32</sup>. The XAFS data were obtained in fluorescence mode with a Lytle detector, and the data for the reference sample were obtained in transmission mode. Typically, the Kapton adhesive tape was used to seal the electrode sheet. In addition, the reference sample was applied evenly onto a special adhesive tape after grinding down. Data manipulation and curve fitting were accomplished using the ATHENA and ARTEMIS modules of the Demeter software packages.

### Computational details

The Vienna Ab-initio Simulation Package (VASP 5.2)<sup>46–49</sup> was employed to carry out the theoretical calculations. The generalized gradient approximation functional (GGA)<sup>50</sup> with the PBE was employed for the exchange correlation function. To accurately describe the 3d and 5d orbitals, the Hubbard U correction was employed. The effective U values are 3.3 eV for Pt-5d<sup>51</sup>, 4.7 eV for Zn-3d<sup>52</sup>, and 4.2 eV for Ti-3d<sup>53</sup>. The plane wave basis is employed for the wave functions expanded, with a cutoff energy of 400 eV, and the Fermi scheme (energy smearing of 0.1 eV) is used to estimate the electron occupancy. For reciprocal space, Monkhorst-Pack grid with 3×3×1 k-point mesh is employed for the slab calculation<sup>54</sup>. The energy (1.0 ×10<sup>-6</sup> eV/atom) and force (0.01 eV/Å) convergence criterion were employed for the structural relaxation. The Crystal Orbital Hamilton Population (COHP) is employed to analysis the chemical bond (strength and bonding/anti-bonding state), which is carried out by the program of LOBSTER<sup>55–57</sup>. For COHP, the negative and positive values are the bonding and anti-bonding state, respectively. The integral of COHP, i.e. ICOHP, can be used to estimate the bond strength, whose value is more negative, the stronger of the bond will be shown. The anatase-TiO<sub>2</sub> (Angle, α = β = γ = 90°; lattice, A = B = 3.7760 Å, C = 9.4860 Å; space group, I41) was employed to construct the slab model, i.e. a supercell of (3×6)-TiO<sub>2</sub> (101) slab including 108 Ti atoms and 216 O atoms with lattice length of 16.33 Å×22.656 Å and a vacuum layer of 15 Å along the c direction. The three layers of TiO<sub>2</sub> slab were employed in the model. For adsorption process, the bottom layer in the model was fixed to simulate the bulk phase, while the other layers were allowed to relax through the structural optimization. The surface energy of TiO<sub>2</sub> (101) slab is ~-0.50 eV (the middle layer was fixed, while the top and bottom layers were allowed to relax), which is estimated by the following formula (1):

$$E_{sur} = \frac{E_{slab} - nE_{bulk}}{2A} \quad (1)$$

where  $E_{slab}$  and  $E_{bulk}$  are the total energies for slab and bulk model,  $n$  is the number of bulk formula units in the slab,  $A$  is the surface area, while a factor of 2 is due to two surfaces for slab model. The negative  $E_{sur}$  suggests the TiO<sub>2</sub> (101) is stable. The spin polarization was considered in the calculation, while the optimized magnetic moment for each atom is shown in Supplementary Table 5.

The adhesion energy ( $\Delta E_{ade}$ ) of Zn and Pt single atoms is estimated by the formula:

$$\Delta E_{ade} = E_{total} - E_{Zn} - E_{Pt} \quad (2)$$

where  $E_{total}$  is the total energy of Zn/Pt SATs, while  $E_{Zn}$  and  $E_{Pt}$  are the chemical potential of Zn and Pt atoms based on the bulk phase, respectively. The calculated adhesion energy (formula (2)) for Zn and Pt single atoms of Zn/Pt SATs is  $-1.94$  eV, suggesting that the structure of Pt and Zn co-adsorption is stable.

In this work, the DFT model is employed to treat  $^1O_2$  through controlling the spin arrangement of O atoms in  $O_2$  during the reaction. If possible, to obtain a more accurate reaction mechanism and quantitative explanation, the method based on multireference state is recommended.

### **$O_2$ generation in vitro**

Briefly, 1 mL of Zn/Pt SATs ( $1 \text{ mg mL}^{-1}$ ) was injected in the  $H_2O_2$  solution ( $100 \text{ mM}$ ) in airtight environment. The dissolved oxygen values were recorded by JPB-608 portable dissolved oxygen meter every 10 s.

### **$^1O_2$ generation in vitro**

The production of  $^1O_2$  was measured by singlet oxygen sensor green (SOSG) fluorescence probe. In brief, the mixture of Zn/Pt SATs ( $500 \text{ } \mu\text{g mL}^{-1}$ ) and SOSG solution with or without  $H_2O_2$  solution was exposed to US irradiation ( $1 \text{ W cm}^{-2}$ ,  $1 \text{ MHz}$ ,  $50\%$  duty cycle) in the dark. Then, the fluorescence at  $525 \text{ nm}$  was measured by fluorescence spectrophotometer. In addition, the trapping agent 2,2,6,6-Tetramethylpiperidine (TEMP) was also used to detect the production of  $^1O_2$  in aqueous dispersion of D-TiO<sub>2</sub>, Zn SATs, Pt SATs, or Zn/Pt SATs with the same concentration of  $500 \text{ } \mu\text{g mL}^{-1}$  under US irradiation ( $1 \text{ W cm}^{-2}$ ,  $1 \text{ MHz}$ ,  $50\%$  duty cycle,  $5 \text{ min}$ ) by an ESR spectrometer.

### **OH generation in vitro**

POD-like activity of Zn/Pt SATs was studied by monitoring the absorbance change at  $665 \text{ nm}$  of 3,3',5,5'-TMB. Briefly, Zn/Pt SATs ( $1000 \text{ } \mu\text{g mL}^{-1}$ ),  $H_2O_2$  ( $0.97 \text{ mol L}^{-1}$ ), and TMB ( $10 \text{ mg mL}^{-1}$ , dissolved in dimethyl sulfoxide (DMSO)) were added in PBS solution ( $3 \text{ mL}$ ,  $\text{pH} = 6.5$ ). The absorbance change curve was recorded by UV-vis spectrophotometer. The production of  $\cdot\text{OH}$  under US irradiation was measured by hydroxyphenyl fluorescein (HPF) fluorescence probe. In brief, the Zn/Pt SATs ( $500 \text{ } \mu\text{g mL}^{-1}$ ),  $H_2O_2$  ( $10 \text{ mM}$ ), and HPF solution were added to  $1 \text{ mL}$  PBS solution ( $\text{pH} = 6.5$ ) exposed to US irradiation ( $1 \text{ W cm}^{-2}$ ,  $1 \text{ MHz}$ ,  $50\%$  duty cycle,  $5 \text{ min}$ ) in the dark. Then, the fluorescence in  $515 \text{ nm}$  was measured by fluorescence spectrophotometer. In addition, another trapping agent 5,5-dimethyl-1-pyrroline-N-oxide (DMPO) was also used to detect production of  $\cdot\text{OH}$  in aqueous dispersion of Zn/Pt SATs exposed to US irradiation for  $5 \text{ min}$  and then detect by an ESR spectrometer.

### **Detection of GSH consumption**

GSH solution ( $10 \text{ mM}$ ) was added to Zn/Pt SATs ( $500 \text{ } \mu\text{g mL}^{-1}$ ) solution. Then, DTNB solution ( $1.5 \text{ mg mL}^{-1}$ ) was added at desired time points, the mixed solution was recorded by UV-vis spectrophotometer.

### **CCK-8 assay**

**Biocompatibility of Zn/Pt SATs.** L929 cells were seeded in 96-well plates with 8000 cells of  $100 \text{ } \mu\text{L}$  RPMI 1640 medium per well and grown in  $5\% \text{ CO}_2$  at  $37 \text{ }^\circ\text{C}$  overnight. Subsequently, Zn/Pt SATs with a series of concentrations ( $0$ ,  $25$ ,  $50$ ,  $100$ ,  $200$ , and  $400 \text{ } \mu\text{g mL}^{-1}$ ) were added to the medium, and the cells were incubated in  $5\% \text{ CO}_2$  at  $37 \text{ }^\circ\text{C}$  for  $24 \text{ h}$ . Finally, the L929 cells were washed with PBS and the cell viability was measured by Cell Counting Kit-8 assay kit. The absorbance of each well was assessed by Thermo Multiskan FC microplate reader.

**In vitro cytotoxicity of Zn/Pt SATs.** 4T1 cells were seeded in 96-well plates with 8000 cells of  $100 \text{ } \mu\text{L}$  RPMI 1640 medium per well and grown in  $5\% \text{ CO}_2$  at  $37 \text{ }^\circ\text{C}$  overnight. Subsequently, Zn/Pt SATs with a series of concentrations ( $0$ ,  $25$ ,  $50$ ,  $100$ ,  $200$ , and  $400 \text{ } \mu\text{g mL}^{-1}$ ) and  $H_2O_2$  ( $100 \text{ } \mu\text{M}$ ) were added to the medium ( $\text{pH} = 6.5$ ). After incubating for  $4 \text{ h}$ , the cells were treated with and without US irradiation. Then, the cells were incubated for an extra  $24 \text{ hours}$ . Finally, the 4T1 cells were washed with PBS, and the cytotoxic effects of Zn/Pt SATs were measured by Cell Counting Kit-8 assay kit. The absorbance of each well was assessed by Thermo Multiskan FC microplate reader.

### **Cell imaging**

The cell fluorescence images were obtained by confocal laser scanning microscopy (Nikon Eclipse Ni-E, Japan). Briefly, 4T1 cells were seeded in 12-well plates with  $10^5$  cells per well in RPMI 1640 medium and grown in  $5\% \text{ CO}_2$  at  $37 \text{ }^\circ\text{C}$  overnight. The 4T1 cells were then untreated or treated with US irradiation ( $1 \text{ W cm}^{-2}$ ,  $1 \text{ MHz}$ ,  $50\%$  duty cycle,  $2 \text{ min}$ ), Zn/Pt SATs ( $400 \text{ } \mu\text{g mL}^{-1}$ ), and Zn/Pt SATs ( $400 \text{ } \mu\text{g mL}^{-1}$ ) + US irradiation ( $1 \text{ W cm}^{-2}$ ,  $1 \text{ MHz}$ ,  $50\%$  duty cycle,  $2 \text{ min}$ ) under co-incubation of  $H_2O_2$  ( $100 \text{ } \mu\text{M}$ ) at  $\text{pH} 6.5$ .

**Live/dead cell staining analysis.** After treatment as the above description, Calcein-AM ( $10 \text{ } \mu\text{g mL}^{-1}$ ) and PI ( $5 \text{ } \mu\text{g mL}^{-1}$ ) were added to each well to dye the viable cells and dead cells.

**Intracellular ROS generation.** After being treated according to the above conditions, the DCFH-DA was added to every well for  $20 \text{ min}$ .

**Detection of mitochondrial membrane potential.** After treated according to the above conditions, the cells were stained with JC-1 for  $20 \text{ min}$  at  $37 \text{ }^\circ\text{C}$ .

**LPO detection.** After treated according to the above conditions, the Liperfluo probe ( $5 \text{ } \mu\text{M}$ ) was added to the mixture incubated for  $30 \text{ min}$ . Afterward, the cell nuclei were stained with Hoechst for another  $10 \text{ min}$  at  $37 \text{ }^\circ\text{C}$ .

### **Intracellular GSH consumption**

4T1 cells were seeded in 12-well plates with  $10^5$  cells of  $1 \text{ mL}$  RPMI 1640 medium per well and grown in  $5\% \text{ CO}_2$  at  $37 \text{ }^\circ\text{C}$  overnight. Subsequently, the cells were incubated with Zn/Pt SATs ( $0$ ,  $25$ ,  $100$ , and  $400 \text{ } \mu\text{g mL}^{-1}$ ) solution. The remnant GSH was detected by GSH assay kits.

### **Western blot assays**

4T1 cells ( $10^5$  cells per well) were seeded in 12-well plates and grown in  $5\% \text{ CO}_2$  at  $37 \text{ }^\circ\text{C}$  overnight. The cells were untreated or treated with US irradiation ( $1 \text{ W cm}^{-2}$ ,  $1 \text{ MHz}$ ,  $50\%$  duty cycle,  $2 \text{ min}$ ), Zn/Pt SATs ( $400 \text{ } \mu\text{g mL}^{-1}$ ), and Zn/Pt SATs ( $400 \text{ } \mu\text{g mL}^{-1}$ ) + US irradiation ( $1 \text{ W cm}^{-2}$ ,  $1 \text{ MHz}$ ,  $50\%$  duty cycle,  $2 \text{ min}$ ). Then, the cells were collected by trypsin and lysed by RIPA buffer. The protein was quantified by BCA protein assay. Next, the proteins were separated by sodium dodecyl sulfate-polyacrylamide gel electrophoresis (SDS-PAGE). After electrophoresis, the proteins were moved to a polyvinylidene fluoride membrane and blocked by  $5\%$  dried skimmed milk for  $1 \text{ h}$ . The proteins (GPX4) were detected by respectively incubating the membranes with the corresponding primary antibody (Servicebio) overnight at  $4 \text{ }^\circ\text{C}$  and then cultivated with the secondary antibody (Servicebio) for  $1 \text{ h}$  at room temperature. Finally, the membrane was detected by chemiluminescence.

### **Cell apoptosis analysis**

4T1 cells ( $10^5$  cells per well) were seeded in 12-well plates and grown in  $5\% \text{ CO}_2$  at  $37 \text{ }^\circ\text{C}$  overnight. The cells were collected after treated according to the above conditions. Subsequently,  $5 \text{ } \mu\text{L}$  of Annexin V

and 5  $\mu\text{L}$  of PI were added into the mixture and incubated for 15 min in the dark. Finally, the binding buffer was added and operated to detect cell apoptosis by flow cytometry (guava easyCyte™).

### In vivo biocompatibility of Zn/Pt SATs

4T1 tumor-bearing mice were intravenously injected with Zn/Pt SATs (100  $\mu\text{L}$ , 20 mg  $\text{kg}^{-1}$ ). The mice were sacrificed at 4 h, 12 h, 24 h, and 48 h, respectively. The tumor tissues and main organs containing the heart, liver, spleen, lung, and kidney were excised and weighed. Then, the tumor tissues and major organs were digested by aqua regia. Finally, Ti content in tumor tissues and major organs was measured by ICP-MS.

### Tumor suppression experiments of Zn/Pt SATs

The tumor-bearing BALB/c mice were randomly assigned into four groups (five mice each group): (1) PBS (100  $\mu\text{L}$ ), (2) US irradiation (1  $\text{W cm}^{-2}$ , 1 MHz, 50% duty cycle, 5 min), (3) Zn/Pt SATs, and (4) Zn/Pt SATs+US irradiation (1  $\text{W cm}^{-2}$ , 1 MHz, 50% duty cycle, 5 min). After intravenous injection for 24 h, US irradiation was carried out at the tumor region in groups 2 and 4. The tumor sizes and body weight were recorded every 2 d.

### GPX4, TUNEL, and H&E staining of tumor

The excised tumors after different treatments were stained with fluorochrome-conjugated anti-mouse GPX4 antibody, terminal deoxynucleotidyl TUNEL, and H&E, respectively. These sections were photographed by fluorescence microscope.

### Statistical analysis

All experiments were performed at least three times unless otherwise noted, and the results are expressed as mean  $\pm$  S.D. The significance of the difference was decided through two-tailed *t* test. Significance is indicated by *P* values.

### Reporting summary

Further information on research design is available in the Nature Portfolio Reporting Summary linked to this article.

### Data availability

All data are available in the main text, Supplementary Information, or Source Data file. If any raw data files are needed in another format, they are available from the corresponding author upon request. Source data are provided with this paper.

### References

- Gong, F. et al. Preparation of  $\text{TiH}_{1.924}$  nanodots by liquid-phase exfoliation for enhanced sonodynamic cancer therapy. *Nat. Commun.* **11**, 3712 (2020).
- Wen, D., Li, K., Deng, R., Feng, J. & Zhang, H. Defect-rich glassy  $\text{IrTe}_2$  with dual enzyme-mimic activities for sono-photosynergistic-enhanced oncotherapy. *J. Am. Chem. Soc.* **145**, 3952–3960 (2023).
- Li, G. et al. Titanium sulfide nanosheets serve as cascade bioreactors for  $\text{H}_2\text{S}$ -mediated programmed gas-sonodynamic cancer therapy. *Adv. Sci.* **9**, 2201069 (2022).
- Liu, K. et al. Triarylboron-doped acenethiophenes as organic sonosensitizers for highly efficient sonodynamic therapy with low phototoxicity. *Adv. Mater.* **34**, 2206594 (2022).
- Li, G. et al. Fluorinated chitosan to enhance transmucosal delivery of sonosensitizer-conjugated catalase for sonodynamic bladder cancer treatment post-intravesical instillation. *ACS Nano* **14**, 1586–1599 (2020).
- Xiao, Z. et al. State of the art advancements in sonodynamic therapy (SDT): metal-organic frameworks for SDT. *Chem. Eng. J.* **449**, 137889 (2022).
- You, C. et al. Self-assembled aza-boron-dipyrromethene for ferroptosis-boosted sonodynamic therapy. *Angew. Chem. Int. Ed.* **61**, e202210174 (2022).
- Lai, Y., Lu, N., Ouyang, A., Zhang, Q. & Zhang, P. Ferroptosis promotes sonodynamic therapy: a platinum(II)-indocyanine sonosensitizer. *Chem. Sci.* **13**, 9921–9926 (2022).
- Wang, H. et al. A Mxene-derived redox homeostasis regulator perturbs the Nrf2 antioxidant program for reinforced sonodynamic therapy. *Chem. Sci.* **13**, 6704–6714 (2022).
- Yang, Y. et al. Emerging sonodynamic therapy-based nanomedicines for cancer immunotherapy. *Adv. Sci.* **10**, 2204365 (2023).
- Geng, B. et al. Near-infrared phosphorescent carbon dots for sonodynamic precision tumor therapy. *Nat. Commun.* **13**, 5735 (2022).
- Zhou, Y. et al. Oxygen-deficient tungsten oxide ( $\text{WO}_x$ ) nanobelts with PH-sensitive degradation for enhanced sonodynamic therapy of cancer. *ACS Nano* **16**, 17242–17256 (2022).
- Liang, C. et al. A highly potent ruthenium(II)-sonosensitizer and sonocatalyst for in vivo sonotherapy. *Nat. Commun.* **12**, 5001 (2021).
- Bai, S. et al. Ultrasmall iron-doped titanium oxide nanodots for enhanced sonodynamic and chemodynamic cancer therapy. *ACS Nano* **14**, 15119–15130 (2020).
- Liu, S. et al. Construction of multiform hollow-structured covalent organic frameworks via a facile and universal strategy for enhanced sonodynamic cancer therapy. *Angew. Chem. Int. Ed.* **62**, e202301831 (2023).
- Zhang, M. et al. Two-dimensional Mxene-originated in situ nanosensitizer generation for augmented and synergistic sonodynamic tumor nanotherapy. *ACS Nano* **16**, 9938–9952 (2022).
- Dong, Z. et al. Synthesis of  $\text{CaCO}_3$ -based nanomedicine for enhanced sonodynamic therapy via amplification of tumor oxidative stress. *Chem* **6**, 1391–1407 (2020).
- Yang, Z. et al. Conferring  $\text{BiVO}_4$  nanorods with oxygen vacancies to realize enhanced sonodynamic cancer therapy. *Angew. Chem. Int. Ed.* **61**, e202209484 (2022).
- Cao, Z. et al. Macrophage-targeted sonodynamic/photothermal synergistic therapy for preventing atherosclerotic plaque progression using  $\text{CuS/TiO}_2$  heterostructured nanosheets. *ACS Nano* **16**, 10608–10622 (2022).
- Zhao, Y. et al. Platinum-titania Schottky junction as nanosonosensitizer, glucose scavenger, and tumor microenvironment-modulator for promoted cancer treatment. *ACS Nano* **16**, 12118–12133 (2022).
- Wang, X. et al. Ultrafine titanium monoxide ( $\text{TiO}_{1+x}$ ) nanorods for enhanced sonodynamic therapy. *J. Am. Chem. Soc.* **142**, 6527–6537 (2020).
- Dong, Y. et al. 2D piezoelectric  $\text{Bi}_2\text{MoO}_6$  nanoribbons for GSH-enhanced sonodynamic therapy. *Adv. Mater.* **33**, 2106838 (2021).
- Zhao, Y. et al. Piezotronic effect-augmented  $\text{Cu}_{2-x}\text{O-BaTiO}_3$  sonosensitizers for multifunctional cancer dynamic therapy. *ACS Nano* **16**, 9304–9316 (2022).
- Zhang, R. et al. A phase engineering strategy of perovskite-type  $\text{ZnSnO}_3:\text{Nd}$  for boosting the sonodynamic therapy performance. *Adv. Funct. Mater.* **33**, 2300522 (2023).
- Liang, S. et al. A novel Pt- $\text{TiO}_2$  heterostructure with oxygen-deficient layer as bilaterally enhanced sonosensitizer for synergistic chemo-sonodynamic cancer therapy. *Adv. Funct. Mater.* **30**, 1908598 (2020).
- Gong, F. et al. Ultrasmall oxygen-deficient bimetallic oxide  $\text{MnWO}_x$  nanoparticles for depletion of endogenous GSH and enhanced sonodynamic cancer therapy. *Adv. Mater.* **31**, 1900730 (2019).
- Wang, Y. et al. Oxygen-deficient molybdenum oxide nanosensitizers for ultrasound-enhanced cancer metalloimmunotherapy. *Angew. Chem. Int. Ed.* **62**, e202215467 (2023).

28. Liang, S. et al. A robust narrow bandgap vanadium tetrasulfide sonosensitizer optimized by charge separation engineering for enhanced sonodynamic cancer therapy. *Adv. Mater.* **33**, 2101467 (2021).
29. Cao, F. et al. Self-adaptive single-atom catalyst boosting selective ferroptosis in tumor cells. *ACS Nano* **16**, 855–868 (2022).
30. Chang, M. et al. Cu single atom nanozyme based high-efficiency mild photothermal therapy through cellular metabolic regulation. *Angew. Chem. Int. Ed.* **61**, e202209245 (2022).
31. Cao, F. et al. An enzyme-mimicking single-atom catalyst as an efficient multiple reactive oxygen and nitrogen species scavenger for sepsis management. *Angew. Chem. Int. Ed.* **59**, 5108–5115 (2020).
32. Sarma, B. B., Maurer, F., Doronkin, D. E. & Grunwaldt, J. D. Design of single-atom catalysts and tracking their fate using operando and advanced X-ray spectroscopic tools. *Chem. Rev.* **123**, 379–444 (2023).
33. Finzel, J. et al. Limits of detection for EXAFS characterization of heterogeneous single-atom catalysts. *ACS Catal.* **13**, 6462–6473 (2023).
34. Zhou, X. et al. A single-atom manipulation approach for synthesis of atomically mixed nanoalloys as efficient catalysts. *Angew. Chem. Int. Ed.* **59**, 13568–13574 (2020).
35. Chen, Q. et al. Single atom-doped nanosonosensitizers for mutually optimized sono/chemo-nanodynamic therapy of triple negative breast cancer. *Adv. Sci.* **10**, 2206244 (2023).
36. Peng, C., Pang, R., Li, J. & Wang, E. Current advances on the single-atom nanozyme and its bio-applications. *Adv. Mater.* **36**, 2211724 (2023).
37. Zhang, X. et al. Identifying and tailoring C-N coupling site for efficient urea synthesis over diatomic Fe-Ni catalyst. *Nat. Commun.* **13**, 5337 (2022).
38. Zhou, X. et al. Dual-site single-atom catalysts with high performance for three-way catalysis. *Adv. Mater.* **34**, 2201859 (2022).
39. Li, M. et al. Proximity electronic effect of Ni/Co diatomic sites for synergistic promotion of electrocatalytic oxygen reduction and hydrogen evolution. *Adv. Funct. Mater.* **33**, 2210867 (2023).
40. Ma, C. B. et al. Guided synthesis of a Mo/Zn dual single-atom nanozyme with synergistic effect and peroxidase-like activity. *Angew. Chem. Int. Ed.* **61**, e202116170 (2022).
41. Tian, R. et al. Se-containing MOF coated dual-Fe-atom nanozymes with multi-enzyme cascade activities protect against cerebral ischemic reperfusion injury. *Adv. Funct. Mater.* **32**, 2204025 (2022).
42. Liu, M. et al. Tuning the site-to-site interaction in Ru-M (M = Co, Fe, Ni) diatomic electrocatalysts to climb up the volcano plot of oxygen electroreduction. *ACS Nano* **16**, 10657–10666 (2022).
43. Liang, S. et al. Conferring Ti-based MOFs with defects for enhanced sonodynamic cancer therapy. *Adv. Mater.* **33**, 2100333 (2021).
44. Chang, M. et al. Single-atom Pd nanozyme for ferroptosis-boosted mild-temperature photothermal therapy. *Angew. Chem. Int. Ed.* **60**, 12971–12979 (2021).
45. Yuan, M. et al. Rational design of platinum-bismuth sulfide Schottky heterostructure for sonocatalysis-mediated hydrogen therapy. *Adv. Mater.* **35**, 2209589 (2023).
46. Perdew, J. P., Burke, K. & Ernzerhof, M. Generalized gradient approximation made simple. *Phys. Rev. Lett.* **77**, 3865–3868 (1996).
47. Kresse, G. & Furthmüller, J. Efficiency of ab-initio total energy calculations for metals and semiconductors using a plane-wave basis set. *Comput. Mater. Sci.* **6**, 15–50 (1996).
48. Kresse, G. & Hafner, J. Ab initio molecular dynamics for liquid metals. *Phys. Rev. B* **47**, 558–561 (1993).
49. Kresse, G. & Hafner, J. Ab initio molecular-dynamics simulation of the liquid-metal–amorphous-semiconductor transition in germanium. *Phys. Rev. B* **49**, 14251–14269 (1994).
50. Kresse, G. & Furthmüller, J. Efficient iterative schemes for ab initio total-energy calculations using a plane-wave basis set. *Phys. Rev. B* **54**, 11169–11186 (1996).
51. Buchwald, J. & Hennes, M. Adsorption and diffusion of Au, Pt, and Co adatoms on SrTiO<sub>3</sub>(001) surfaces: a density functional theory study. *Surf. Sci.* **701**, 121683 (2020).
52. Janotti, A. & Segev, D. & Van de Walle, C.G. Effects of cation d states on the structural and electronic properties of III-nitride and II-oxide wide-band-gap semiconductors. *Phys. Rev. B* **74**, 045202 (2006).
53. Wang, L. et al. Facet-dependent photocatalytic decomposition of N<sub>2</sub>O on the anatase TiO<sub>2</sub>: A DFT study. *Nanoscale* **10**, 6024–6038 (2018).
54. Monkhorst, H. J. & Pack, J. D. Special points for Brillouin-zone integrations. *Phys. Rev. B* **13**, 5188–5192 (1976).
55. Dronskowski, R. & Blöchl, P. E. Crystal orbital Hamilton populations (COHP): energy-resolved visualization of chemical bonding in solids based on density-functional calculations. *J. Phys. Chem.* **97**, 8617–8624 (1993).
56. Deringer, V. L., Tchougréeff, A. L. & Dronskowski, R. Crystal orbital Hamilton population (COHP) analysis as projected from plane-wave basis sets. *J. Phys. Chem. A* **115**, 5461–5466 (2011).
57. Maintz, S., Deringer, V. L., Tchougréeff, A. L. & Dronskowski, R. LOBSTER: a tool to extract chemical bonding from plane-wave based DFT. *J. Comput. Chem.* **37**, 1030–1035 (2016).

## Acknowledgements

This work was supported by financial aid from the National Key Research and Development Program of China (2021YFF0701800, J.F. and 2022YFB3503700, J.F.), the National Natural Science Foundation of China (22020102003, H.Z.), the Youth Innovation Promotion Association of Chinese Academy of Sciences (Y201947, J.F.), and Jilin Province Science and Technology Development Plan Project (20220101063JC, J.F.).

## Author contributions

D.W. and J.F. designed the research. D.W., R.D., K.L., and J.F. performed the research. D.W., J.F., R.D., and K.L. analyzed the data. K.L. performed theoretical calculations. D.W., J.F., K.L., and H.Z. conceived the manuscript. H.Z. supervised the research.

## Competing interests

The authors declare no competing interests.

## Additional information

**Supplementary information** The online version contains supplementary material available at <https://doi.org/10.1038/s41467-024-53488-8>.

**Correspondence** and requests for materials should be addressed to Jing Feng, Kai Li or Hongjie Zhang.

**Peer review information** *Nature Communications* thanks the anonymous reviewers for their contribution to the peer review of this work. A peer review file is available.

**Reprints and permissions information** is available at <http://www.nature.com/reprints>

**Publisher's note** Springer Nature remains neutral with regard to jurisdictional claims in published maps and institutional affiliations.

**Open Access** This article is licensed under a Creative Commons Attribution-NonCommercial-NoDerivatives 4.0 International License, which permits any non-commercial use, sharing, distribution and reproduction in any medium or format, as long as you give appropriate credit to the original author(s) and the source, provide a link to the Creative Commons licence, and indicate if you modified the licensed material. You do not have permission under this licence to share adapted material derived from this article or parts of it. The images or other third party material in this article are included in the article's Creative Commons licence, unless indicated otherwise in a credit line to the material. If material is not included in the article's Creative Commons licence and your intended use is not permitted by statutory regulation or exceeds the permitted use, you will need to obtain permission directly from the copyright holder. To view a copy of this licence, visit <http://creativecommons.org/licenses/by-nc-nd/4.0/>.

© The Author(s) 2024